PAPER

Check for updates

Unlocking dual Mn³⁺/Mn⁴⁺ emissions in garnet phosphors for WLED and plant growth lighting applications†

Khuat Thi Thu,[a] Vu Dinh Huan,[a] Nguyen Tu, [iD] *[b] Do Quang Trung, [iD] [b] Nguyen Van Du,[b] Nguyen Van Quang,[c] Ta Ngoc Bach,[d] Le Tien Ha,[e] Nguyen Duy Hung,[f] Dao Xuan Viet,[f] Nguyen Tri Tuan,[g] Nguyen Minh Hieu, [iD] [a] Manh Trung Tran [iD] *[a] and Pham Thanh Huy [iD] [a]

Garnet-based lattices (A₃B₅O₁₂) have emerged as promising hosts for Mn co-doping due to their wide band gap and robust mechanical properties. However, challenges in stabilizing Mn³⁺, balancing Mn³⁺/Mn⁴⁺ emissions, and optimizing synthesis for thermal stability and efficiency have limited practical applications. In this study, $Gd_3Ga_5O_{12}$ (GGG) garnet was synthesized with Mn³⁺ and Mn⁴⁺ co-doping *via* a simple solid-state reaction. The incorporation of Mn ions into octahedral $[GaO_6]$ sites and optimizing the synthesis condition to enhance photoluminescence (PL) properties were investigated. The phosphor achieved 100% color purity, 0.32 eV activation energy, 20.0% internal quantum efficiency, and a 0.0408 ms lifetime. A prototype pc-LED was fabricated, demonstrating that the Mn³⁺/Mn⁴⁺-doped Garnet-based phosphor can be used as potential WLED and plant growth LED components. These results provide insights into stabilizing Mn³⁺, controlling Mn³⁺/Mn⁴⁺ balance, and improving thermal stability for advanced lighting applications.

1. Introduction

Lighting plays a pivotal role in modern society, influencing a wide range of domains, including industry, broad-based applications, and daily human activities. Among the most notable technological advancements of the 21st century are light-emitting diodes (LEDs) utilizing phosphor materials, celebrated for their numerous advantages.[1,2] Commercial white light-emitting diodes (WLEDs) based on YAG:Ce³⁺ phosphor coated on GaN chip LED (460 nm) exhibit a deficiency in the red region of the emission spectrum. This limitation results in a low

[a]Faculty of Materials Science and Engineering, Phenikaa University, Yen Nghia, Ha-Dong District, Hanoi 10000, Vietnam. E-mail: trung.tranmanh@phenikaa-uni.edu.vn

[b]Faculty of Fundamental Science, Phenikaa University, Yen Nghia, Ha-Dong District, Hanoi 10000, Vietnam. E-mail: tu.nguyen@phenikaa-uni.edu.vn

[c]Department of Chemistry, Hanoi Pedagogical University, 2, Phuc Yen, Vinh Phuc, Vietnam

[d]Institute of Materials Science, Vietnam Academy of Science and Technology, 18 Hoang Quoc Viet Street, Cau Giay District, Hanoi 10000, Vietnam

[e]Institute of Science and Technology, TNU-University of Sciences, Thai Nguyen, 250000, Vietnam

[f]Faculty of Electronic Materials and Components, School of Materials Science and Engineering, Hanoi University of Science and Technology (HUST), 01 Dai Co Viet Street, Hanoi 10000, Vietnam

[g]College of Science, Cantho University, 3/2, Ninh Kieu, Cantho 94000, Vietnam

† Electronic supplementary information (ESI) available. See DOI: https://doi.org/10.1039/d5ra00345h

color rendering index (CRI) and a highly correlated color temperature (CCT).[3,4] To address these challenges and achieve a full-visible-spectrum emission in WLEDs, extensive research has focused on developing red-emitting phosphors.[5–7] Notable examples include $Li_2Ca_2Mg_2Si_2N_6$:Eu²⁺,[8] which emits at 638 nm and enhances the CRI of WLEDs to as high as 91, as well as Ca_2LuSbO_6:Eu³⁺ (λ_{em} = 613 nm)[9] and $Sr_2LiScB_4O_{10}$: Eu³⁺ (λ_{em} = 617 nm).[10] However, despite the success of Eu³⁺-doped materials, recent research increasingly focuses on Mn-based ions, particularly Mn³⁺ and Mn⁴⁺, which offer unique advantages for red-emission phosphors due to their partially filled d-orbitals. Mn³⁺ (with d⁴ configuration) exhibits red and far-red emission *via* ⁵E′ and ⁵E″ transitions, induced by Jahn–Teller splitting of the ²E ground state.[11–13] In contrast, Mn⁴⁺ (with a d³ configuration) emits deep red light through ²E → ⁴A₂ and ⁴T₂ → ⁴A₂ transitions.[14,15] Co-doping these ions is particularly promising, as their complementary emission properties enable the creation of a broader and tunable red-emission spectrum. The fact that Mn is cost-effective and environmentally friendly further enhances its appeal. However, challenges remain in controlling the emission profiles of Mn³⁺ and Mn⁴⁺, which are highly sensitive to fabrication conditions. A major challenge in achieving the coexistence of Mn³⁺ and Mn⁴⁺ in phosphor materials is the precise regulation of manganese valence states during synthesis.[16,17] Mn³⁺ is particularly unstable, as it readily oxidizes to Mn⁴⁺ under oxidizing conditions or reduces to Mn²⁺ in a reducing environment.[18,19] This instability complicates the

control of the Mn^{3+}/Mn^{4+} ratio, which is essential for fine-tuning the red emission properties of the phosphor.

Garnet-based lattices ($A_3B_5O_{12}$) are highly promising for Mn co-doping due to their wide band gap and excellent mechanical properties. Among these, $Y_3Al_5O_{12}$ (YAG) has been extensively studied as a host for Mn^{4+}, which can substitute for Al^{3+} in octahedral sites with minimal lattice distortion.[20] In contrast, $Gd_3Ga_5O_{12}$ garnet, despite its similar structural properties, has received relatively little attention.[21] The $Gd_3Ga_5O_{12}$ lattice, characterized by Ga^{3+} ions ($r = 0.62$ Å, CN = 6), is well-suited to accommodate both Mn^{3+} ions ($r = 0.65$ Å, CN = 6)[22,23] and Mn^{4+} ions ($r = 0.53$ Å, CN = 6),[22,24] making it an ideal candidate for co-doping.[13] Incorporating both Mn^{3+} and Mn^{4+} into the $Gd_3Ga_5O_{12}$ lattice enables the exploration of their unique emission characteristics and offers the potential to fine-tune the red-emission spectrum by controlling the Mn^{3+}/Mn^{4+} ratio.[25] Studies by L. Marciniak and K. Trejgis have investigated this co-doping strategy Mn^{3+} and Mn^{4+} in the $Gd_3Ga_5O_{12}$ lattice,[11] while S. Kuck analyzed the PL properties of Mn^{3+}-doped $Gd_3Ga_5O_{12}$.[13] Despite progress, the full potential of $Gd_3Ga_5O_{12}$:Mn for LEDs remains unrealized, with challenges in balancing Mn^{3+}/Mn^{4+} emissions and optimizing synthesis for red emission, stability, and efficiency.[11] Precise annealing, charge compensation, and non-radiative loss suppression are crucial to stabilizing Mn^{3+} and advancing Mn-doped garnet phosphors for next-generation WLEDs.

This study employs a simple solid-state reaction technique to synthesize the dual red and far-red emitting (Mn^{3+}, Mn^{4+})-activated $Gd_3Ga_5O_{12}$ phosphors. The effects of experimental conditions on crystal structure, morphology, elemental composition, bonding characteristics, and photoluminescent properties of (Mn^{3+}, Mn^{4+})-activated $Gd_3Ga_5O_{12}$ phosphors are systematically investigated. Key performance metrics are evaluated, including color purity, lifetime, thermal stability, and internal quantum efficiency of the synthesized phosphors. Additionally, a prototype-tested LED device was successfully fabricated by coating a layer of the optimized phosphor onto the surface of a NUV-chip LED (310 nm).

2.   Experimental

2.1.   Synthesis of the $Gd_3Ga_5O_{12}$:Mn phosphors

A series of $Gd_3Ga_5O_{12}$:x%Mn ($x = 0.2$–2.0) was fabricated by a simple solid-state reaction method. The starting materials included Gd_2O_3 (99.99% purity, Merck), Ga_2O_3 (99.99% purity, Merck), and $MnCl_2 \cdot 4H_2O$ (99.9% purity, Merck) were magnetically stirred in 100 ml of deionized water at room temperature. The mixture was then dried at 150 °C in the air for 10 hours, ground by a high-energy planetary ball milling at 200 rpm for 30 minutes, and annealed at 1000–1300 °C for 5 hours in the air to receive the final $Gd_3Ga_5O_{12}$:x%Mn phosphors. The maximum annealing temperature was set at 1300 °C, as higher temperatures lead to melting phenomena and partial decomposition of the garnet phase into perovskite ($REGaO_3$) and Ga_2O_3 liquidus, compromising phase purity and structural integrity.[26] The experimental process is illustrated in Fig. S1.†

2.2.   Characterization

The crystal structure of the samples was analyzed by X-ray diffraction (XRD) patterns measured over a 2θ range of 25° to 75° with a D8 Advance diffractometer. High-resolution transmission electron microscopy (HRTEM) was performed on a JEM2500SE microscope (JEOL) operating at 200 kV to provide further structural insights. Structural visualization was created using VESTA software. The samples' surface morphology and element composition were examined using field emission scanning electron microscopy (FESEM) images and the energy dispersion spectrum (EDS) using JSM-7600F equipment. Bonding energies of the ions were characterized by X-ray photoelectron spectroscopy (XPS) using a Thermo Scientific XPS system with an Al Kα X-ray source. The optical properties of the samples were evaluated through PL and photoluminescence excitation (PLE) spectra, obtained with a NanoLog spectrophotometer (Horiba) equipped with a 450 W xenon discharge lamp as the excitation source. The PL decay times were measured using a fluorescence spectrophotometer (Agilent Cary Eclipse).

2.3.   LED packaging

The optimized $Gd_3Ga_5O_{12}$:Mn phosphors were used to produce a prototype of an LED device. Initially, a polydimethylsiloxane (PDMS) solution (Dow Corning OE-7340 Optical Encapsulant) was obtained by blending an elastomer and a hardener in a 1 : 1 ratio. Then, the PDMS and the optimized phosphor were combined at a mass ratio of 1 : 4 and thoroughly mixed using a planetary mixer (Kurabo Mazerustar KK-V300SS) for 270 seconds. The resulting mixture was then applied to the top surface of a 310 nm LED chip using an i-DRS310A Desktop Dispensing System. Finally, the phosphor-coated LED was cured in an oven (ASONE AVO-310SB-D) at 150 °C for 4 hours to remove any residual solvents. The optical properties of the fabricated LED chip were characterized using a Gamma Scientific GS-1290 spectroradiometer (RadOMA).

3.   Results and discussion

3.1.   XRD and HRTEM analysis

Fig. 1a shows the XRD patterns of the $Gd_3Ga_5O_{12}$:0.2%Mn samples annealed at different temperatures in the air for 5 hours. At an annealing temperature of 1100 °C, the XRD pattern reveals the initial formation of the $Gd_3Ga_5O_{12}$ phase. As the annealing temperature increases, the intensity of the diffraction peaks associated with the $Gd_3Ga_5O_{12}$ phase becomes more pronounced, accompanied by a narrowing of the peaks. These indicate a significant improvement in crystalline with increasing temperature. At 1300 °C, all diffraction peaks corresponding to the cubic $Gd_3Ga_5O_{12}$ phase (PDF # 13-0493) are distinctly observed at $2\theta = 26.54°, 28.68°, 31.96°, 35.06°, 39.49°, 45.65°, 50.53°, 52.79°, 54.97°, 59.13°, 67.00°, 68.81°, 70.71°$. The peaks correspond to the (321), (400), (420), (422), (521), (611), (444), (640), (642), (800), (840), (842), (664) crystal planes, respectively.[27,28] The above result confirms that the single-phase $Gd_3Ga_5O_{12}$ is most effectively stabilized at 1300 °C compared to lower annealing temperatures.
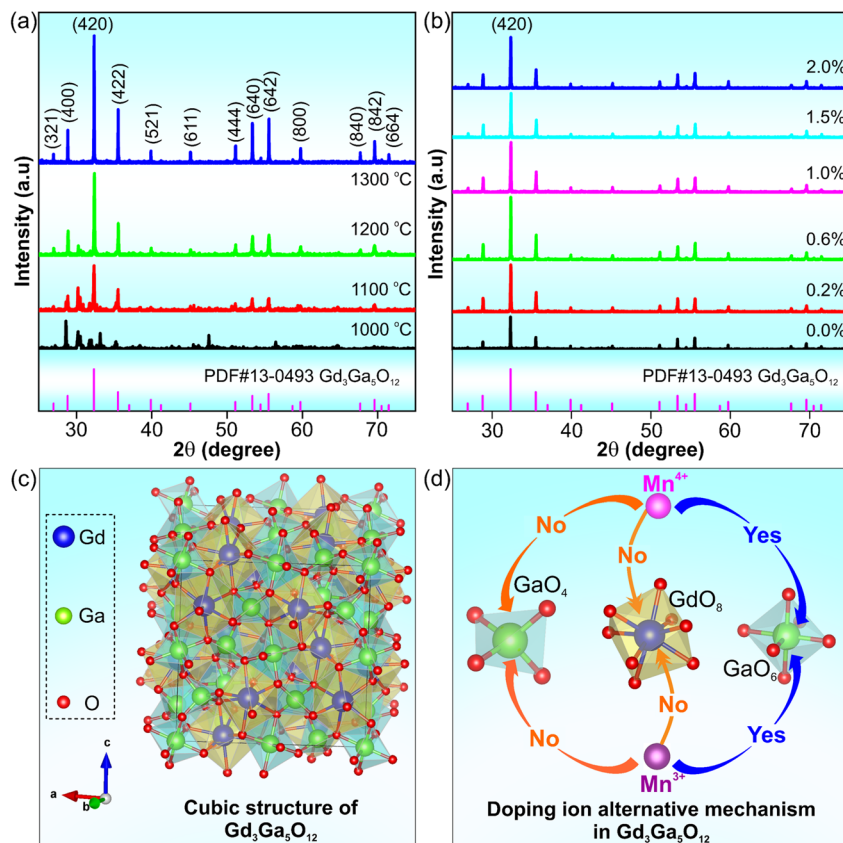
Fig. 1 XRD patterns of (a) $Gd_3Ga_5O_{12}$:0.2% Mn phosphors annealed at various temperatures and (b) $Gd_3Ga_5O_{12}$:x% Mn ($x = 0.0-2.0$) phosphors annealed at 1300 °C (c) cubic structure of the $Gd_3Ga_5O_{12}$ lattice modeled using VESTA software and (d) preferred substitution of Mn^{3+} and Mn^{4+} ions for Ga^{3+} ions [GaO_6] sites in the $Gd_3Ga_5O_{12}$ lattice.

Fig. 1b shows the XRD patterns of the $Gd_3Ga_5O_{12}$:x%Mn ($x = 0.0-2.0$) samples, annealed at 1300 °C in air for 5 hours. Notably, no significant differences in the XRD patterns suggest that doping concentration does not affect the crystal structure of $Gd_3Ga_5O_{12}$.[29–31] Fig. 1c illustrates the cubic structure of the $Gd_3Ga_5O_{12}$ lattice, visualized using VESTA software. It is well-known that the difference in radii between the dopant and substituted ions (D_r) can be calculated using the following eqn (1):[32]

$$D_r = \frac{R_s(CN) - R_d(CN)}{R_s(CN)} \times 100 \qquad (1)$$

where R_s and R_d are the radii of the substituted and doping ions, respectively, and CN is their coordination number. It is reported that ion substitution occurs only when the D_r value is within 30%.[32] For the $Gd_3Ga_5O_{12}$:Mn phosphors, the ionic radii in the host lattice are as follows: $r = 0.62$ Å (Ga^{3+}, CN = 6), $r = 0.47$ Å (Ga^{3+}, CN = 4), and $r = 1.053$ Å (Gd^{3+}, CN = 8). For Mn ions, $r = 0.53$ Å (Mn^{4+}, CN = 6),[33,34] and $r = 0.645$ Å (Mn^{3+}, CN = 6).[35] This indicates that only the Ga^{3+} ion (CN = 6) in the octahedral site can be replaced by Mn^{3+} (CN = 6, $D_r = 4$%) or Mn^{4+} ions (CN = 6, $D_r = 13$%). Additionally, Mn^{4+} ions can substitute Ga^{3+} in both octahedral ($D_r = 13$%) and tetrahedral ($D_r = 15$%) sites in the lattice. Substituting larger ions shifts XRD peaks to lower 2θ angles, whereas smaller ions shift peaks to higher 2θ angles.[36,37]

Mn^{4+} is predominantly stabilized in octahedral coordination, as confirmed by previous studies,[33,34] while Mn^{3+} primarily occupies octahedral sites in garnets, consistent with existing literature.[13,22] Thus, both Mn^{3+} and Mn^{4+} are most likely substituting Ga^{3+} at the octahedral [GaO_6] sites, as shown in Fig. 1d. The ionic radius differences between Mn^{3+} and Mn^{4+} induce localized lattice distortions, which may influence optical properties such as emission wavelength and intensity.[31,38]

Fig. 2 shows the Rietveld refinement of the $Gd_3Ga_5O_{12}$:x%Mn ($x = 0.0-2.0$) phosphors annealed at 1300 °C for 5 hours. Table 1 demonstrates a strong agreement between the theoretical and experimental data, with low χ^2 values ranging from 1.14 to 1.45. As Mn doping increases, both the lattice parameter, a, and cell volume, V, increase from 12.3756 Å and 1895.3909 Å^3 at 0.0% Mn to 12.3766 Å and 1895.8504 Å^3 at 2.0% Mn. Furthermore, the refinement indicators R_p and R_{wp} decrease higher Mn doping levels, indicating improved refinement accuracy. These findings confirm the reliability of the Rietveld analysis and align with the X-ray diffraction results, validating the structural modifications in the $Gd_3Ga_5O_{12}$ lattice caused by Mn doping.

Fig. 3a–d presents the TEM image, selected area electron diffraction (SAED) pattern, and high-resolution TEM (HRTEM) image of the $Gd_3Ga_5O_{12}$:0.2%Mn sample annealed at 1300 °C for 5 hours in the air. The SAED pattern in Fig. 3b shows diffraction rings corresponding to the crystallite planes of the
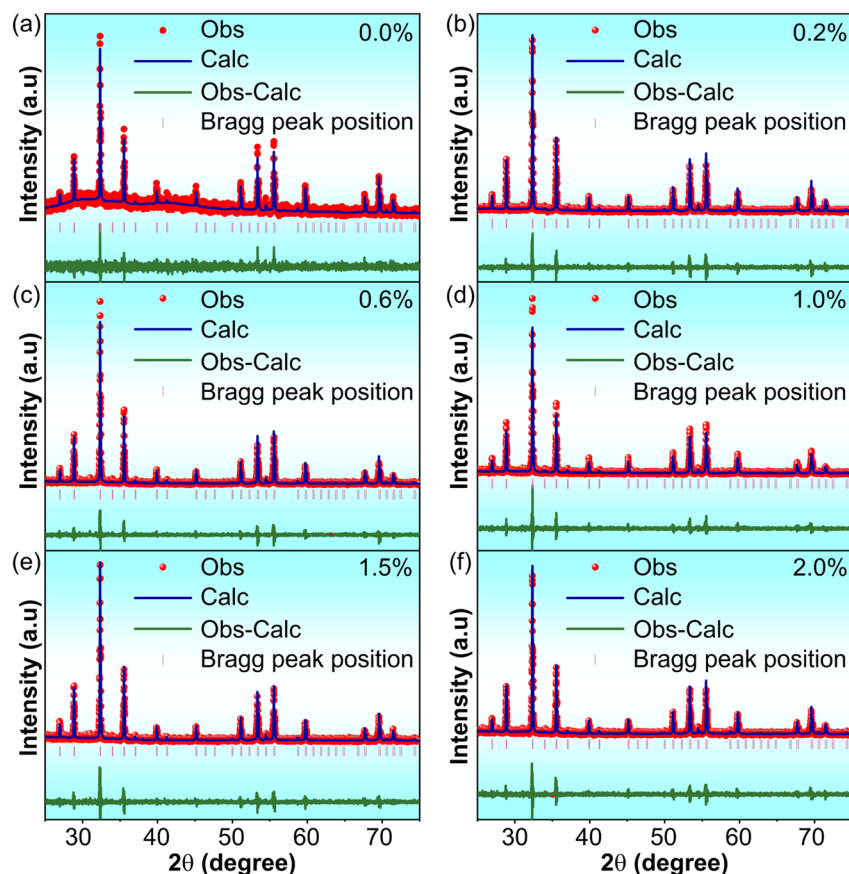
Fig. 2 Rietveld refinement for the $Gd_3Ga_5O_{12}$:x%Mn (x = 0.0–2.0) phosphors annealed at 1300 °C for 5 hours in air.

$Gd_3Ga_5O_{12}$ structure. The fast Fourier transform (FFT) image in the inset of Fig. 3c reveals symmetric point pairs that align with the $Gd_3Ga_5O_{12}$ phase. In Fig. 3d, the inverse fast Fourier transform (IFFT) of the marked point pair indicates an orderly atomic arrangement with a d-spacing of 0.308 nm, corresponding to the (400) plane of the $Gd_3Ga_5O_{12}$.[31,39] Additionally, the XRD data demonstrates the presence of the (400) plane with an interplanar spacing of d = 3.09 Å, which aligns well with previous reports.[29–31] These results confirm that the synthesized phosphor is a single-phase $Gd_3Ga_5O_{12}$ structure.

3.2. FESEM image and EDS spectra investigation

Fig. 4a–d shows the FESEM images of $Gd_3Ga_5O_{12}$:0.2%Mn samples annealed at various temperatures in air for 5 hours. As the annealing temperature increases, the particle size grows, reflecting enhanced crystallization of the $Gd_3Ga_5O_{12}$ structure.[1]

The sample annealed at 1300 °C shows the largest particles, approximately 2 μm, making it suitable for LED chip fabrication.[37] The EDS spectrum (Fig. 4e) confirms the presence of Gd (14.06 at%), Ga (23.33 at%), O (62.50 at%), and Mn (0.11 at%), with no impurities detected. Elemental mapping (Fig. 4f–k) corroborates these findings, revealing a uniform distribution of these elements across the sample. These results confirm that the sample achieved high purity and a particle size closely aligned with the standard requirements for phosphor applications.

3.3. XPS spectra investigation

Fig. 5 presents the XPS spectra of the $Gd_3Ga_5O_{12}$:Mn sample, providing a comprehensive analysis of the chemical composition and valence states of the constituent elements. The survey spectrum (Fig. 5a) confirms the presence of all expected elements without detectable impurities, consistent with the

Table 1 Refinement parameters obtained from Rietveld analysis of the $Gd_3Ga_5O_{12}$:x% Mn (x = 0.0–2.0) phosphors annealed at 1300 °C

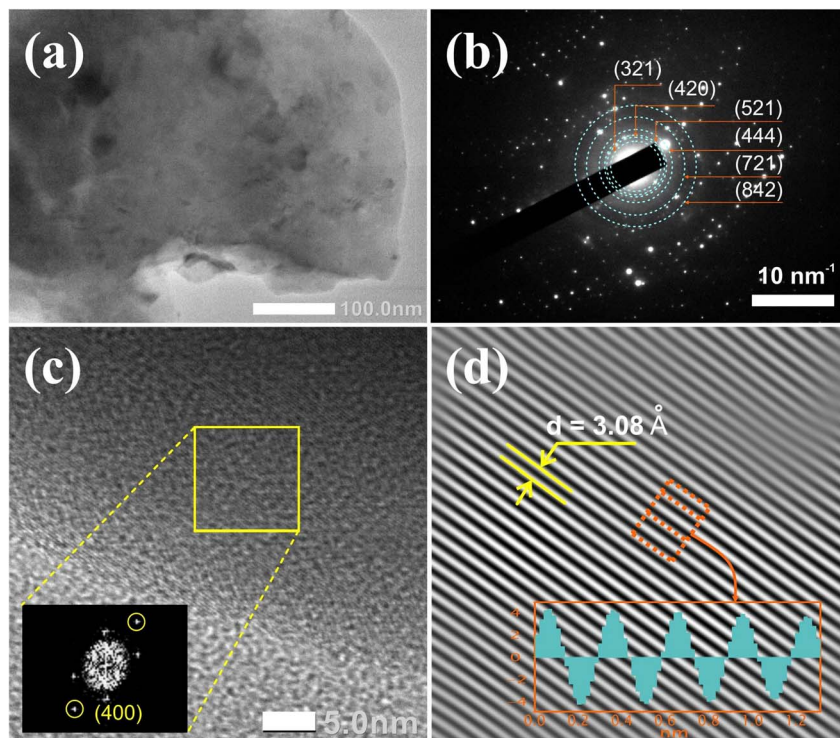| Doping concentration (mol%)	R_p (%)	R_{wp} (%)	χ^2	Lattice parameter $a = b = c$ (Å)	Cell volume V (Å^3)
0.0%	116	61.7	1.14	12.3756	1895.3909
0.2%	62.1	47.9	1.42	12.3760	1895.5747
0.6%	58.2	45.9	1.41	12.3759	1895.5287
1.0%	55.1	46.0	1.35	12.3763	1895.7125
1.5%	68.4	50.9	1.41	12.3765	1895.8045
2.0%	68.0	51.4	1.45	12.3766	1895.8504

Fig. 3 (a) TEM image, (b) selected area electron diffraction (SAED) pattern, (c) high-resolution TEM (HRTEM) image and (d) IFFT images and corresponding lattice plane fringes of the $Gd_3Ga_5O_{12}$:0.2%Mn sample annealed at 1300 °C for 5 hours in air.

earlier elemental mapping results.[30] The C 1s spectrum, peaking at 285.7 eV (Fig. 5b), serves as a reference for energy shift corrections.[40,41] The Gd 4d spectrum (Fig. 5c) shows two prominent peaks at 147.6 eV and 142 eV, representing Gd $4d_{3/2}$ and Gd $4d_{5/2}$ states of Gd^{3+} ion.[42] The Gd $4d_{5/2}$ state bonding energy can be decomposed into five peaks at 145.8 eV, 144.8 eV,
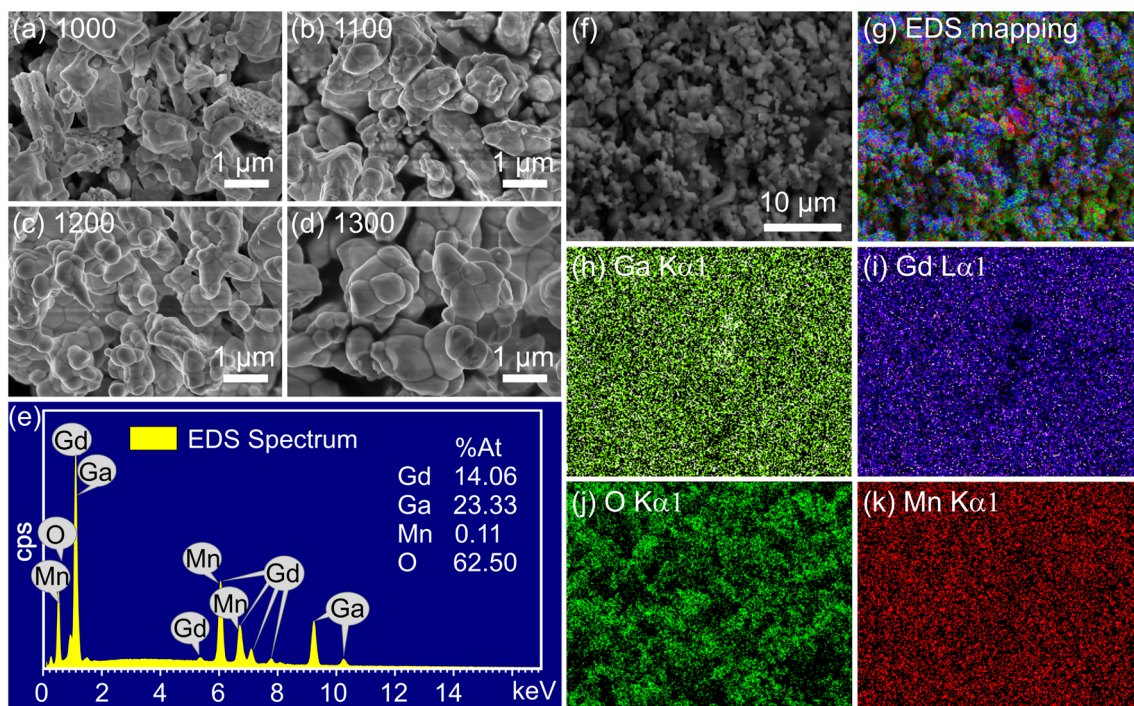

Fig. 4 (a–d) FESEM images of the $Gd_3Ga_5O_{12}$:0.2%Mn samples annealed at 1000–1300 °C. (e) EDS elements spectrum and (f) The scanned FESEM of EDS (g–k) EDS mapping spectra of the $Gd_3Ga_5O_{12}$:0.2%Mn sample annealed at 1300 °C.
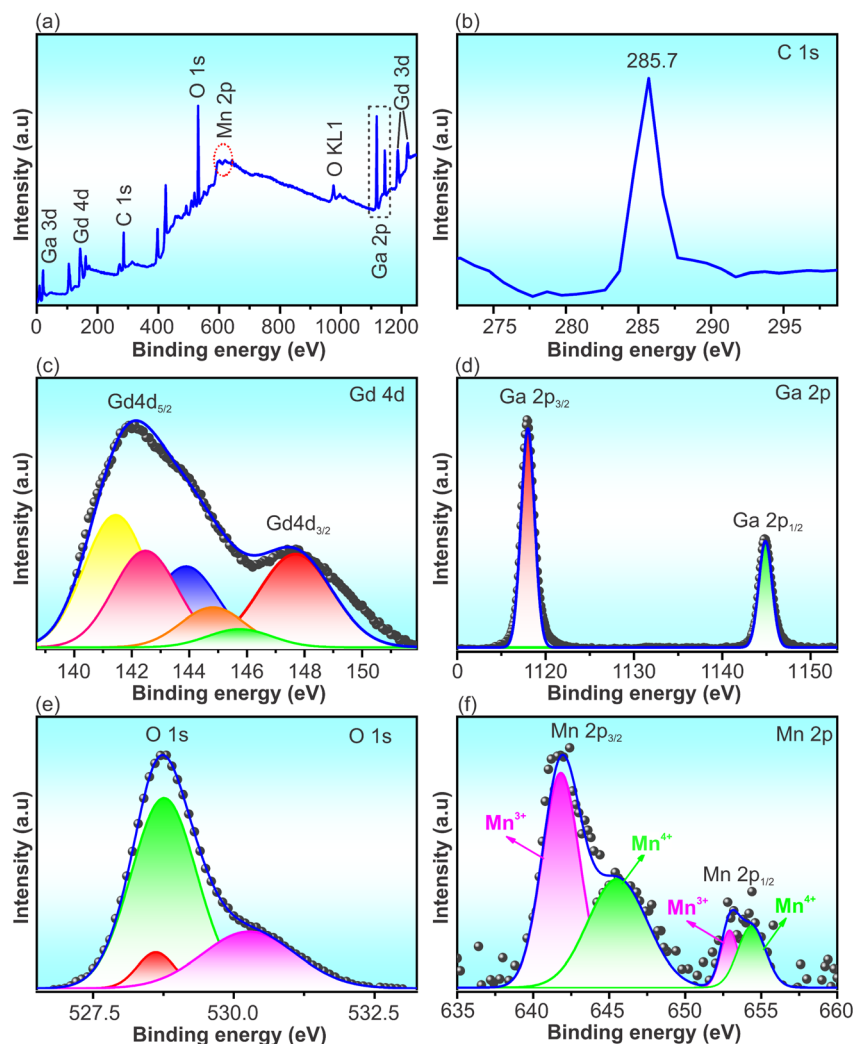
Fig. 5 XPS spectra of $Gd_3Ga_5O_{12}$:0.2%Mn sample: (a) survey spectrum, (b) C 1s, (c) Gd 4d, (d) Ga 2p, (e) O 1s and (f) Mn 2p.

143.9 eV, 142.5 eV and 141.5 eV, attributed to the interaction between the 4d photoholes and valence electrons of the $4f^7$ level.[42–44] The Ga 2p spectrum (Fig. 5d) reveals two peaks at 1117.9 eV and 1144.8 eV, corresponding to the Ga $2p_{3/2}$ and Ga $2p_{1/2}$, respectively.[30,45] The O 1s spectrum (Fig. 5e) consists of three components with peaks at 530.3 eV, 528.7 eV, and 528.6 eV, representing oxygen bonding states associated with the measurement environment, Ga–O and Gd–O bonds, respectively.[30,46] The Mn 2p spectrum (Fig. 5f) reveals two bands, deconvoluted into four peaks at 641.8 eV, 645.4 eV, 653.0, and 654.3 eV.[47,48] The peaks at 641.8 eV and 653.0 eV correspond to the $2p_{3/2}$ and $2p_{1/2}$ states of Mn^{3+} ions, while the peaks at 645.4 eV and 654.3 eV originated from the $2p_{3/2}$ and $2p_{1/2}$ states of Mn^{4+} ions.[47,48] These results indicate the coexistence of Mn^{3+} and Mn^{4+} oxidation states in the $Gd_3Ga_5O_{12}$ lattice.

3.4. Photoluminescence study

Fig. 6a shows the PL spectra of $Gd_3Ga_5O_{12}$:0.2%Mn sample annealed at 1300 °C for 5 hours under excitation at 275 and 450 nm, revealing three deconvoluted emission peaks at 638, 714, and 776 nm, as shown in Fig. 6b and c. The peaks at 638 and 776 nm correspond to the $^5T_2 \rightarrow {}^5E'$ and $^5T_2 \rightarrow {}^5E''$ transitions of the Mn^{3+} ion, respectively, while the 714 nm peak arises from the $^2E \rightarrow {}^4A_2$ transition of Mn^{4+} ions in the $Gd_3Ga_5O_{12}$ lattice.[11–13] This assignment is further substantiated by the presence of fine structure (zero-phonon lines and vibrionics) in the PL spectrum of Mn^{4+} ions (Fig. 6c), which is a defining characteristic of the $^2E \rightarrow {}^4A_2$ transition in Mn^{4+}.[33] The PLE spectra recorded at 638 and 714 nm, shown in Fig. 6d, reveal absorption bands in the NUV and blue-green regions, with distinct peaks at 265, 275, 300, 330, 450, and 525 nm (Fig. 6e and f). The observed Stokes shift from the $^4A_2 \rightarrow E_2$ absorption band further confirms the Mn^{4+} luminescence characteristics.[34] The peaks at 265 and 300 remain attributed to $O^{2-} \rightarrow Mn^{3+}$ [13] and $O^{2-} \rightarrow Mn^{4+}$ [33,34] charge-transfer transition, respectively. Meanwhile, the peaks at 275, 525 and 330 nm in Fig. 6e are assigned the $^5E'' \rightarrow {}^5T_2$ transition, $^5E' \rightarrow {}^5T_2$ transition of Mn^{3+} ions[13,22] and $^4A_2 \rightarrow {}^4T_1$ transition of Mn^{4+} ions. The PLE spectrum measured at 714 nm (Fig. 6f) exhibits six fitted peaks at 265, 275, 300, 330, 450 and 525 nm. The 275 and 525 nm peaks reaffirm the Mn^{3+} transitions ($^5E'' \rightarrow {}^5T_2$ and $^5E' \rightarrow {}^5T_2$, respectively),[13,22] whereas the 330 and 450 nm peaks are

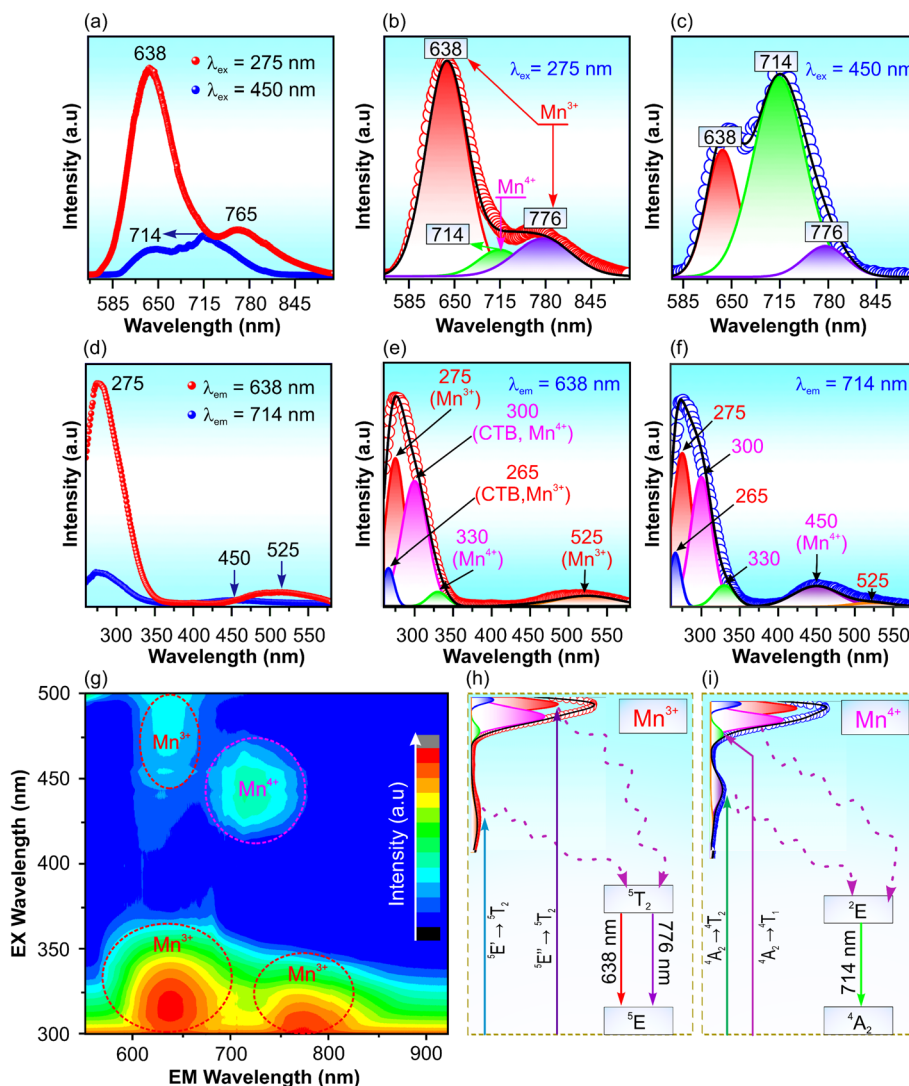**Fig. 6** (a) PL spectrum of $Gd_3Ga_5O_{12}$:0.2%Mn annealed at 1300 °C for 5 hours in air excited at 275 and 450 nm. The fitting PL curves stimulated at (b) 275 nm and (c) 450 nm. (d) PLE spectrum of $Gd_3Ga_5O_{12}$:0.2% Mn annealed at 1300 °C for 5 h in air that monitoring for the 638 and 714 nm emission wavelengths. (e and f) The fitting PLE curves for the 638 and 714 nm emission positions; (g) 3D spectrum of $Gd_3Ga_5O_{12}$:0.2% Mn annealed at 1300 °C. The energy level transitions diagram explaining the absorption and emission process of (h) Mn^{3+} and (i) Mn^{4+}ions in the $Gd_3Ga_5O_{12}$ lattice.

associated with the $^4A_2 \rightarrow {}^4T_1$ and $^4A_2 \rightarrow {}^4T_2$ transitions of Mn^{4+} ions.[33,34] These findings confirm that the observed red and far-red emissions originate from the coexistence of Mn^{3+} and Mn^{4+} ions in the lattice. To further investigate the optical properties of the $Gd_3Ga_5O_{12}$:Mn sample, a 3D spectrum was measured (Fig. 6g). The results indicate that under UV excitation, the PL intensity governed by Mn^{3+}, while blue-light excitation predominantly enhances Mn^{4+} ions emissions. This suggests that the red and far-red emission regions can be tuned by varying the excitation conditions. Finally, a proposed energy-level scheme is provided in Fig. 6h and i that illustrates the absorption and emission mechanisms of Mn^{3+} and Mn^{4+} ions in the $Gd_3Ga_5O_{12}$ lattice.

Fig. 7 reveals key insights into the effect of annealing temperature and doping concentration on the PL properties of $Gd_3Ga_5O_{12}$:Mn ($x = 0.2–2.0$) samples. Under 275 nm excitation

(Fig. 7a), Mn^{3+} emission becomes evident only after the annealing temperatures exceed 1000 °C, with intensity increasing at higher temperatures. The spectral contributions of Mn^{3+} and Mn^{4+} ions were deconvoluted and analyzed in Fig. S2 and Table S1 of the ESI† and presented in the insert of Fig. 7a. It demonstrates a gradual increase in Mn^{3+} and Mn^{4+} emission intensities as annealing temperature rises. This is attributed to improved crystallization and enhanced diffusion of impurity ions.[49] Under 450 nm excitation (Fig. 7c), Mn^{4+} emission intensity dominates, and both Mn^{3+} and Mn^{4+} emissions follow a similar increasing trend with annealing temperature (Fig. S3 and Table S2 of ESI† and the inset of Fig. 7c), further supporting the temperature-dependent emission enhancement.

Doping concentration also significantly influences PL intensity. As shown in Fig. 7b and d, the highest PL intensity is
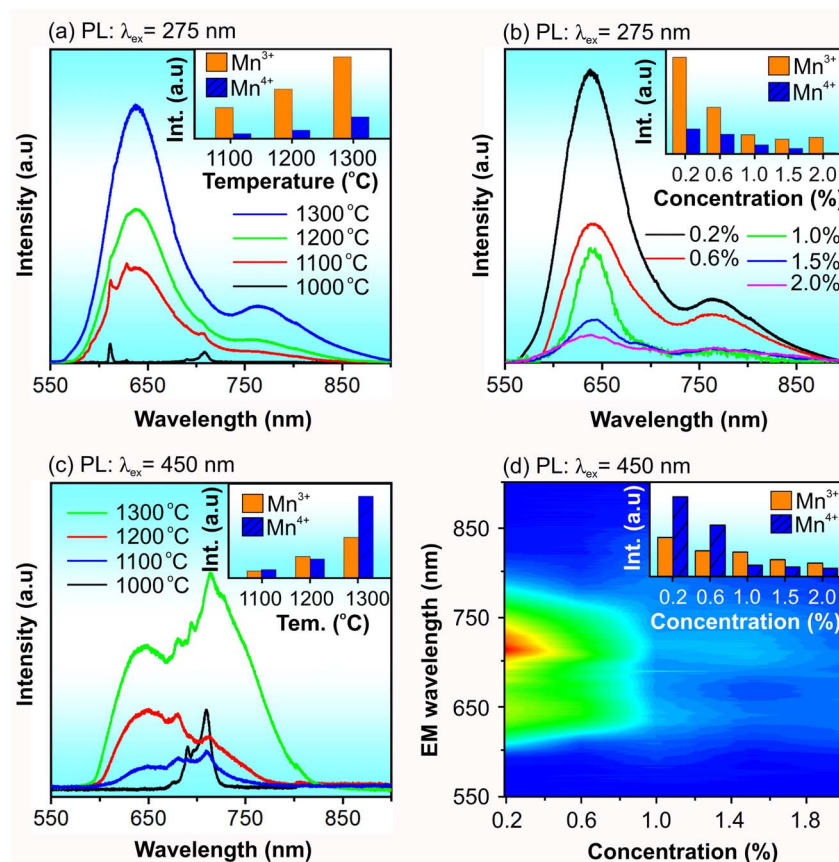
Fig. 7 PL spectra excited at 275 nm of (a) $Gd_3Ga_5O_{12}$:0.2% Mn samples annealed for 5 h in the air at 1000–1300 °C, (b) $Gd_3Ga_5O_{12}$:x%Mn (x = 0.2–2.0) samples annealed for 5 h in the air at 1300 °C and PL spectra excited at 450 nm of (c) $Gd_3Ga_5O_{12}$: 0.2% Mn samples annealed for 5 h in the air at 1000–1300 °C, (d) $Gd_3Ga_5O_{12}$:x%Mn (x = 0.2–2.0) samples annealed for 5 h in the air at 1300 °C. Insets depict integral intensities of Mn^{3+} and Mn^{4+} emissions as a function of annealing temperature and dopant concentration.

achieved at an Mn doping concentration of 0.2% under 275 and 450 nm excitations. Beyond this concentration, PL intensity decreases due to the concentration quenching effect.[50,51] Fitting analyses for Mn^{3+} and Mn^{4+} emissions, shown in Fig. S4 and S5 of the ESI,† confirm that the maximum PL intensity occurs at 0.2% Mn doping. Tables S3 and S4 of the ESI† present the integral intensities of deconvoluted Mn^{3+} and Mn^{4+} emissions for various $Gd_3Ga_5O_{12}$:x% (x = 0.2–2.0) Mn samples, emphasizing the effects of annealing temperature and doping concentration on their PL properties.

3.5. Lifetime, color purity, thermal stability, and internal quantum efficiency of phosphors

The potential application of $Gd_3Ga_5O_{12}$:Mn phosphor was assessed by evaluating the lifetime, color purity, thermal stability, and internal quantum efficiency (IQE). Fig. 8a presents the PL decay under 275 nm excitation wavelength of $Gd_3Ga_5O_{12}$:x%Mn (x = 0.2–2.0) phosphors. Due to the existence of two emission sources from Mn^{3+} and Mn^{4+} ions occupying different lattice sites, all data were well-fitted using a double-exponential model (see Fig. S7†), described by an eqn (2):[50,51]

$$I_T = A_1 \times \exp\left(\frac{-t}{\tau_1}\right) + A_2 \times \exp\left(\frac{-t}{\tau_2}\right) \quad (2)$$

where, I_T represents the emission intensity at time t, with A_1 and A_2 being constants and τ_1 and τ_2 being the lifetimes of the two exponential components. The average lifetime (τ) was calculated using eqn (3):

$$\tau = \frac{A_1\tau_1^2 + A_2\tau_2^2}{A_1\tau_1 + A_2\tau_2} \quad (3)$$

Using this approach, the lifetimes of the samples were determined, with the optimized $Gd_3Ga_5O_{12}$:0.2% Mn sample showing the highest average lifetime of 0.0408 ms. The observed decrease in lifetime with increasing Mn concentration suggests energy transfer among impurity ions, promoting phonon-assisted non-radiative decay rather than PL.[52] As the dopant concentration rises, the reduced distance between Mn ions enhances non-radiative energy transfer mechanisms such as cross-relaxation and energy migration,[50,51] leading to accelerated luminescence decay. Similar findings are also observed in the PL decay for the 714 nm peak under 450 nm excitation in $Gd_3Ga_5O_{12}$:x% Mn (x = 0.2–2.0) samples (Fig. S6 and S8†).
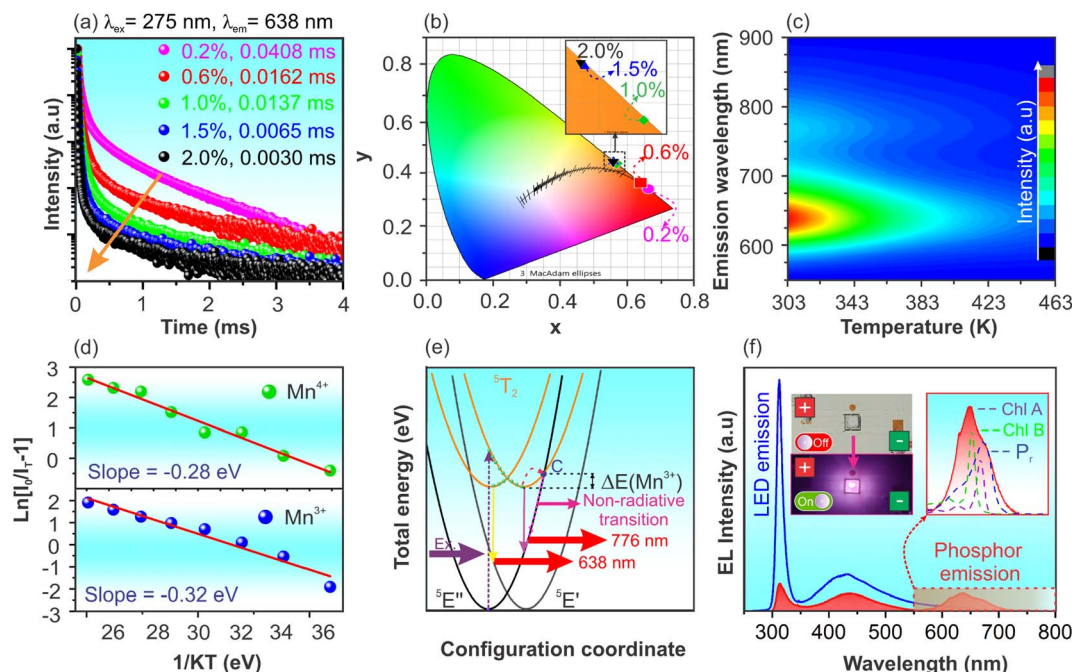
Fig. 8 (a) Lifetime curves for the 638 nm peak under 275 nm excitation, with the arrow indicating the increase of doping concentration; (b) CIE diagram of $Gd_3Ga_5O_{12} : x\%$ Mn ($x = 0.2–2.0$) annealed at 1300 °C in air for 5 h; (c) PL spectrum measured at temperatures in range of room temperature (300 K) to 463 K; (d) correlation between $1/kT$ and $\ln(I_0/I_T - 1)$; (e) schematic representation of the thermal quenching mechanism in $Gd_3Ga_5O_{12}:Mn^{3+}$ and (f) prototype of LED based on 310 nm chip coated $Gd_3Ga_5O_{12}:Mn$ phosphor.

The chromatic coordinates (x, y) of $Gd_3Ga_5O_{12}:x\%Mn$ ($x = 0.2–2.0$) samples annealed at 1300 °C for 5 hours are shown in Fig. 8b, based on the CIE 1931 diagram. The calculated chromatic coordinates (x, y) of samples are listed in Table 2. As shown in Fig. 8b, the samples display red chromatic coordinates close to the boundary of the CIE diagram, demonstrating high color purity. To quantitatively confirm this, the color purity of the sample was further quantified using eqn (4):[53]

$$\text{Color purity} = \frac{\sqrt{(x - x_i)^2 + (y - y_i)^2}}{\sqrt{(x_d - x_i)^2 + (y_d - y_i)^2}} \quad (4)$$

where (x, y), (x_i, y_i) and (x_d, y_d) represent the chromatic coordinates of the phosphor emission, the white illuminant, and the dominant wavelength, respectively, with (x_i, y_i) fixed at (0.3333, 0.3333). The values of (x, y) and (x_d, y_d) are determined from the CIE diagram in Fig. 8b. The calculated color purity for each sample, presented in Table 2, confirms that the color purity of samples exceeds 99.8%.

The temperature-dependent PL spectra of the optimized $Gd_3Ga_5O_{12}:0.2\%Mn$ phosphor ranging from 300 to 463 K are shown in Fig. 8c. A significant decline in PL intensity occurs as the temperature rises, primarily due to thermal quenching.[54,55] The PL spectra measured at various temperatures were also fitted and present in Fig. S9 and Table S5 of the ESI.† At 423 K (150 °C), the PL intensities of Mn^{3+} and Mn^{4+} emissions retain approximately 21.9% and 10.0% of their initial values at 300 K, respectively. To better understand this behavior, the activation energy (E_a) of the sample was estimated using eqn (5):[2,56]

$$I_T = \frac{I_0}{1 + C \times \exp\left(-\dfrac{E_a}{kT}\right)} \quad (5)$$

Here, C is a constant, k is Boltzmann's constant ($k = 8.62 \times 10^{-5}$ eV K^{-1}), I_0 and I_T are the emission intensities at room and measured temperatures, respectively. The eqn (5) can be rewritten in its linearized form as:

Table 2 The chromaticity coordinates, color purity, and lifetime of the $Gd_3Ga_5O_{12}:Mn$ phosphor

Mn concentration (mol%)	Chromaticity coordinates $(x; y)$	Color purity (%)	Lifetime (ms)
0.2	(0.6617; 0.3380)	100	0.0408
0.6	(0.6391; 0.3603)	99.9	0.0162
1.0	(0.5666; 0.4322)	99.8	0.0137
1.5	(0.5579; 0.4409)	99.8	0.0065
2.0	(0.5573; 0.4415)	99.8	0.0030

Table 3 The internal quantum efficiency of the various phosphors based on the Mn^{3+}/Mn^{4+} ions

Phosphors	Excitation wavelength (nm)	Emission wavelength (nm)	Quantum efficiency (QE%)	Ref.
$Gd_3Ga_5O_{12}$:Mn^{3+}	—	—	<5	38
$Gd_3Ga_5O_{12}$:Mn^{3+}, Mn^{4+}			18.2	11
$Gd_3Al_5O_{12}$:Mn^{3+}, Mn^{4+}	—	—	19.0	11
$Y_3Al_5O_{12}$:Mn^{3+}, Mn^{4+}	—	—	22.6	11
$YAlO_3$:Mn^{3+}, Mn^{4+}	—	—	17.8	11
$Lu_3Ga_5O_{12}$:Mn^{3+}, Mn^{4+}	—	—	20.9	11
$Gd_3Al_3Ga_2O_{12}$:Mn	450	628	25.9	63
$Gd_3GaAl_4O_{12}$:Mn	333, 468	630	22.4	31
$Gd_3Al_2Ga_3O_{12}$:Mn	450	628	8.4	63
$Gd_3Al_4Ga_1O_{12}$:Mn	450	628	29.6	63
$Gd_3Ga_5O_{12}$:Mn	**310**	**638**	**20.0**	**This work**

$$\ln\left(\frac{I_0}{I_T} - 1\right) = -\frac{E_a}{kT} \quad (6)$$

By plotting $\ln(I_0/I_T - 1)$ *versus* $1/kT$ (Fig. 8d), the activation energies were determined to be 0.32 eV for Mn^{3+} and 0.28 eV for Mn^{4+} ions, respectively. The obtained activation energy surpasses those of other phosphors, such as $Y_3Ga_3MgSi_{0.5}Ge_{0.5}O_{12}$:0.01$Mn^{4+}$ (0.254 eV),[31] $Sr_2MgGe_2O_7$:Mn^{4+} (0.24 eV),[2] $CaMgAl_{10}O_{17}$:0.02Mn^{4+}, 0.04Mg^{2+} (0.2 eV).[57] Additionally, Mn^{3+}-doped phosphors have garnered significant attention from researchers, as evidenced in several studies.[58-60] However, the activation energy of these phosphors does not appear to have been investigated in detail. The thermal quenching mechanism of $Gd_3Ga_5O_{12}$:Mn can be explained using the configuration coordinate model (Fig. 8e). Upon 275 nm excitation, electrons transition from the $^5E''$ ground state to the $^5T_2$ excited state.[11] The crucial $^5T_2 \rightarrow {}^5E'$ and $^5T_2 \rightarrow {}^5E''$ transitions of the Mn^{3+} ion leads to the red and far-red emissions, respectively. At higher temperatures, electrons at the $^5T_2$ excited state can absorb extra vibration energy to reach the junction of $^5T_2$ and $^5E''$ (point C) and then relax to the $^5E''$ state through non-radiative processes, resulting in a decrease in the PL intensity in the sample.[11]

A prototype pc-LED was obtained by applying the optimized phosphor coating onto the surface of a 310 nm LED chip. The electroluminescence (EL) spectra of the phosphor-coated and uncoated pc-LED device are shown in Fig. 8f. The EL spectrum of the uncoated LED chip displays two emission regions, with peaks at 310 and 438 nm attributed to the emission from the LED chip and the oxidation layer on its surface. In contrast, the EL spectrum of the phosphor-coated LED shows an additional red emission region resulting from the emission of the $Gd_3Ga_5O_{12}$:Mn phosphor. The phosphor's internal quantum efficiency (IQE) could be estimated by eqn (7).[61,62]

$$IQE = \frac{\int I_{em,Vis\text{-}LED} - \int I_{em,Vis\text{-}Chip}}{\int I_{em,NUV\text{-}Chip} - \int I_{em,NUV\text{-}LED}} \times 100\% \quad (7)$$

where $\int I_{em,Vis\text{-}LED}$ and $\int I_{em,Vis\text{-}Chip}$ are the total integrated emission intensities in the visible region of LEDs with and without the phosphor coating layer, respectively. Whereas $\int I_{em,NUV\text{-}LED}$ and $\int I_{em,NUV\text{-}Chip}$ are the total integrated emission intensities in the NUV region of LEDs with and without the phosphor, respectively. The IQE value of the $Gd_3Ga_5O_{12}$:Mn

phosphor is estimated to be approximately 20.0%, which is comparable to the previously reported values (Table 3). The clear images of the LED prototype taken by a digital camera (inset in Fig. 8f) confirm the successful fabrication of the LED device. Notably, the emission spectrum of the tested LED device closely matches the absorption spectra of chlorophyll A (Chl A), chlorophyll B (Chl B), and phytochrome red (Pr), highlighting the strong potential of $Gd_3Ga_5O_{12}$:Mn phosphor for plant growth lighting.[37,51] Additionally, its red emission peak at 638 nm is essential for high-CRI warm WLEDs, making it a valuable red-emitting component in such applications.[3,4] This broad red emission can enhance the color rendering index (CRI) of WLEDs, addressing a key limitation of conventional YAG:Ce-based white LEDs.[15] With its dual-excitation capability, the phosphor offers design flexibility, enabling its use in both warm WLEDs and horticultural lighting, depending on the chosen excitation source.

4. Conclusions

In conclusion, this study successfully synthesized Mn^{3+}/Mn^{4+}-co-doped $Gd_3Ga_5O_{12}$ phosphors, confirming Mn incorporation into the host lattice and demonstrating broad red-to-far-red emission. The optimized phosphor, $Gd_3Ga_5O_{12}$:0.2%Mn annealed at 1300 °C, exhibited a long lifetime (0.0408 ms), high color purity (100%), significant activation energy (0.32 eV), and a quantum efficiency of 20.0%. The luminescence properties were strongly influenced by Mn oxidation states and synthesis conditions, highlighting the importance of precise control over the doping process. A pc-LED prototype incorporating the synthesized phosphor demonstrated its versatility for high-quality white lighting and plant growth applications. Its dual-excitation capability (275 nm and 450 nm) enables flexible integration, enhancing WLED CRI and optimizing deep-red emission for horticultural lighting. These findings support the development of next-generation Mn-doped phosphors with improved stability, efficiency, and multifunctionality.

Data availability

The data supporting this article have been included as part of the ESI.†

Conflicts of interest

The authors declare no conflict of interest.

Acknowledgements

References

1 L. Sun, B. Devakumar, J. Liang, S. Wang, Q. Sun and X. Huang, *J. Alloys Compd.*, 2019, **785**, 312–319.

2 Y. Han, S. Wang, H. Liu, L. Shi, J. Zhang, Z. Zhang, Z. Mao, D. Wang, Z. Mu, Z. Zhang and Y. Zhao, *J. Lumin.*, 2020, **220**, 116968.

3 S. He, F. Xu, T. Han, Z. Lu, W. Wang, J. Peng, F. Du, F. Yang and X. Ye, *Chem. Eng. J.*, 2020, **392**, 123657.

4 W. Chen, Y. Cheng, L. Shen, C. Shen, X. Liang and W. Xiang, *J. Alloys Compd.*, 2018, **762**, 688–696.

5 S. Li, Y. Xia, M. Amachraa, N. T. Hung, Z. Wang, S. P. Ong and R. J. Xie, *Chem. Mater.*, 2019, **31**, 6286–6294.

6 X. Zhang, D. Zhang, Z. Zheng, B. Zheng, Y. Song, K. Zheng, Y. Sheng, Z. Shi and H. Zou, *Dalton Trans.*, 2020, **49**, 17796–17805.

7 D. Wu, C. Shi, J. Zhou, Y. Gao, Y. Huang, J. Ding and Q. Wu, *Chem. Eng. J.*, 2022, **430**, 133062.

8 X. Yang, Y. Zhang, X. Zhang, J. Chen, H. Huang, D. Wang, X. Chai, G. Xie, M. S. Molokeev, H. Zhang, Y. Liu and B. Lei, *J. Am. Ceram. Soc.*, 2020, **103**, 1773–1781.

9 J. Liang, B. Devakumar, L. Sun, G. Annadurai, S. Wang, Q. Sun and X. Huang, *J. Lumin.*, 2019, **214**, 116605.

10 Q. Chen, B. Miao, P. S. Kumar and S. Xu, *Opt. Mater.*, 2021, **116**, 111093.

11 L. Marciniak and K. Trejgis, *J. Mater. Chem. C*, 2018, **6**, 7092–7100.

12 M. Czaja, R. Lisiecki, A. Chrobak, R. Sitko and Z. Mazurak, *Phys. Chem. Miner.*, 2018, **45**, 475–488.

13 S. Kück, S. Hartung, S. Hurling, K. Petermann and G. Huber, *Phys. Rev. B*, 1998, **57**, 2203.

14 S. V. Bulyarskiĭ, A. V. Zhukov and V. V. Prikhod'ko, *Opt. Spectrosc.*, 2003, **94**, 538–544.

15 Y. Li, S. Qi, P. Li and Z. Wang, *RSC Adv.*, 2017, **7**, 38318–38334.

16 E. Jara, R. Valiente, M. Bettinelli and F. Rodríguez, *J. Phys. Chem. C*, 2021, **125**, 27118–27129.

17 M. Gao, Y. Pan, Y. Jin and J. Lin, *RSC Adv.*, 2021, **11**, 760–779.

18 L. Wu, H. Chen, L. Wu, F. Bo, J. Jian, H. Zhang, L. Zheng, Y. Kong, Y. Zhang and J. Xu, *J. Mater. Chem. C*, 2019, **7**, 7096–7103.

19 A. Yadav, B. Tandon and A. Nag, *RSC Adv.*, 2016, **6**, 79153–79159.

20 K. Trejgis and L. Marciniak, *Phys. Chem. Chem. Phys.*, 2018, **20**, 9574–9581.

21 A. Suchocki, S. Biernacki, G. Boulon, A. Brenier, M. Potemski and A. Wysmołek, *Chem. Phys.*, 2004, **298**, 267–272.

22 S. Kück, S. Hartung, S. Hurling, K. Petermann and G. Huber, *Spectrochim. Acta, Part A*, 1998, **54**, 1741–1749.

23 S. Kück, S. Hartung, S. Hurling, K. Petermann and G. Huber, *Phys. Rev. B*, 1998, **57**, 2203.

24 S. V. Bulyarskiĭ, A. V. Zhukov and V. V. Prikhod'ko, *J. Exp. Theor. Phys.*, 2001, **74**, 543–546.

25 M. Nakayama and M. Nogami, *Solid State Commun.*, 2010, **150**, 1329–1333.

26 M. A. Digiuseppe and S. L. Soled, *J. Cryst. Growth*, 1980, **49**, 746–748.

27 A. Luchechko, L. Kostyk, S. Varvarenko, O. Tsvetkova and O. Kravets, *Nanoscale Res. Lett.*, 2017, **12**, 1–6.

28 M. Pang and J. Lin, *J. Cryst. Growth*, 2005, **284**, 262–269.

29 B. Zhang, Y. Feng, Y. Fu, K. Li, M. Liu, B. Zhang, Y. Zhang, J. Sun, C. Zhang, X. Qian, Z. Wang and Q. Liu, *Ceram. Int.*, 2024, **50**, 54753–54761.

30 K. Li, X. Chen, Y. Feng, Y. Fu, P. Chen, J. Lu, B. Wei, L. Zheng, J. Tao and Q. Liu, *J. Alloys Compd.*, 2024, **979**, 173582.

31 L. Dong, L. Zhang, Y. Jia, B. Shao, W. Lu, S. Zhao and H. You, *ACS Appl. Mater. Interfaces*, 2020, **12**, 7334–7344.

32 K. Li, H. Lian, M. Shang and J. Lin, *Dalton Trans.*, 2015, **44**, 20542–20550.

33 S. Adachi, *ECS J. Solid State Sci. Technol.*, 2020, **9**, 016001.

34 S. Adachi, *ECS J. Solid State Sci. Technol.*, 2019, **8**, R183.

35 H. Taguchi, K. Hirota, S. Nishihara, S. Morimoto, K. Takaoka, M. Yoshinaka and O. Yamaguchi, *Phys. Rev. B:Condens. Matter Mater. Phys.*, 2005, **367**, 188–194.

36 K. Li, H. Lian, R. Van Deun and M. G. Brik, *Dyes Pigm.*, 2019, **162**, 214–221.

37 D. Q. Trung, N. Tu, N. V. Quang, M. T. Tran, N. V. Du, P. T. Huy, N. Tu, N. V. Quang, M. T. Tran, N. V. Du and P. T. Huy, *J. Alloys Compd.*, 2020, **845**, 156326.

38 S. Kück, *Appl. Phys. B:Lasers Opt.*, 2001, **72**, 515–562.

39 F. P. Yu, D. R. Yuan, X. L. Duan, S. Y. Guo, X. Q. Wang, X. F. Cheng and L. M. Kong, *J. Alloys Compd.*, 2008, **465**, 567–570.

40 S. T. Jackson and R. G. Nuzzo, *Appl. Surf. Sci.*, 1995, **90**, 195–203.

41 P. S. Bagus, C. Sousa and F. Illas, *J. Chem. Phys.*, 2016, **145**, 144303.

42 N. Ullah, M. Imran, K. Liang, C. Z. Yuan, A. Zeb, N. Jiang, U. Y. Qazi, S. Sahar and A. W. Xu, *Nanoscale*, 2017, **9**, 13800–13807.

43 N. Zhang, D. Chen, F. Niu, S. Wang, L. Qin and Y. Huang, *Sci. Rep.*, 2016, **6**, 1–11.

44 T. B. Thiede, M. Krasnopolski, A. P. Milanov, T. De Los Arcos, A. Ney, H. W. Becker, D. Rogalla, J. Winter, A. Devi and R. A. Fischer, *Chem. Mater.*, 2011, **23**, 1430–1440.

45 L. Kong, J. Ma, C. Luan, W. Mi and Y. Lv, *Thin Solid Films*, 2012, **520**, 4270–4274.

46 P. N. Meitei, B. Moirangthem, C. Ngangbam, M. W. Alam and N. K. Singh, *J. Mater. Sci.:Mater. Electron.*, 2022, **33**, 10705–10714.

47 J. Zha, C. He, F. Chen, H. Wang, B. Dong, L. Liu, M. Xia, C. Deng, Q. Li, Y. Lu and H. Chen, *J. Fluoresc.*, 2024, 1–12.

48 M. Wang, K. Chen, J. Liu, Q. He, G. Li and F. Li, *Catalysts*, 2018, **8**, 138.

49 M. T. Tran, D. Q. Trung, N. Tu, D. D. Anh, N. V Du, N. V Quang, N. T. Huyen, D. X. Viet, N. D. Hung and P. T. Huy, *J. Alloys Compd.*, 2021, **884**, 1–13.

50 N. Tu, N. Van Quang, N. Van Du, D. Q. Trung, T. N. Bach, N. D. Hung, D. X. Viet, L. T. Ha, N. M. Hieu, M. T. Tran and P. T. Huy, *J. Mol. Struct.*, 2024, **1316**, 139004.

51 N. T. Huyen, N. Tu, N. Van Quang, D. Quang Trung, M. T. Tran, N. Van Du, N. D. Hung, D. X. Viet, N. D. Trung Kien and P. T. Huy, *ACS Appl. Electron. Mater.*, 2022, **4**, 4322–4331.

52 Z. Zhou, Y. Li, M. Xia, Y. Zhong, N. Zhou and H. T. (Bert) Hintzen, *Dalton Trans.*, 2018, **47**, 13713–13721.

53 R. Naik, S. C. Prashantha, H. Nagabhushana, S. C. Sharma, H. P. Nagaswarupa and K. M. Girish, *J. Alloys Compd.*, 2016, **682**, 815–824.

54 Y. Tian, *J. Solid State Light.*, 2014, **1**, 1–15.

55 Y. Wei, L. Cao, L. Lv, G. Li, J. Hao, J. Gao, C. Su, C. C. Lin, H. S. Jang, P. Dang and J. Lin, *Chem. Mater.*, 2018, **30**, 2389–2399.

56 S. Wang, J. Cai, R. Pang, H. Wu, Y. Luo, T. Tan, W. Yuan, L. Jiang, C. Li and H. Zhang, *Dalton Trans.*, 2021, **50**, 5666–5675.

57 Y. Yan, C. Luo, S. Ling, J. Liang, S. Liao and Y. Huang, *Opt. Mater.*, 2022, **132**, 112818.

58 J. M. Gonçalves, M. Stefanski, R. Tomala, A. Musialek, B. Cichy, M. Bettinelli and W. Strek, *J. Phys. Chem. C*, 2025, **129**, 2204–2210.

59 Q. Chen, L. Shang, H. Xu, C. Ma and C. K. Duan, *J. Phys. Chem. C*, 2021, **125**, 21780–21790.

60 J. H. You, R. C. Wang, F. Han, R. Guo and X. W. Liu, *Rare Met.*, 2018, **37**, 439–446.

61 D. Q. Trung, N. V. Quang, M. T. Tran, N. V. Du, N. Tu, N. D. Hung, D. X. Viet, D. D. Anh and P. T. Huy, *Dalton Trans.*, 2021, **50**, 9037–9050.

62 I. Mackevic, J. Grigorjevaite, M. Janulevicius and A. Linkeviciute, *Opt. Mater.*, 2019, **89**, 25–33.

63 B. Sun, B. Jiang, J. Fan, L. Zhang and L. Zhang, *J. Am. Ceram. Soc.*, 2022, **106**, 513–526.